ALMA CN Zeeman Observations of AS 209: Limits on Magnetic Field Strength and Magnetically Driven Accretion Rate

Rachel E. Harrison[1] , Leslie W. Looney[1] , Ian W. Stephens[2,3] , Zhi-Yun Li[4], Richard Teague[3] , Richard M. Crutcher[1],
Haifeng Yang[5] , Erin G. Cox[6] , Manuel Fernández-López[7] , and Hiroko Shinnaga[8]

[1] Department of Astronomy, University of Illinois, Urbana, IL 61801, USA; reh3@illinois.edu
[2] Department of Earth, Environment and Physics, Worcester State University, Worcester, MA 01602, USA
[3] Center for Astrophysics | Harvard & Smithsonian, Cambridge, MA 02138, USA
[4] Department of Astronomy, University of Virginia, Charlottesville, VA 22903, USA
[5] Institute for Advanced Study, Tsinghua University, Beijing, 100084, People's Republic of China
[6] Center for Interdisciplinary Exploration and Research in Astrophysics (CIERA), Northwestern University, Evanston, IL 60208, USA
[7] Instituto Argentino de Radioastronomía (CCT-La Plata, CONICET; CICPBA), Villa Elisa, Buenos Aires, Argentina
[8] Department of Physics and Astronomy, Graduate School of Science and Engineering, Kagoshima University, Amanogawa Galaxy Astronomy Research Center
(AGARC), Kagoshima 890-0065, Japan

Abstract

While magnetic fields likely play an important role in driving the evolution of protoplanetary disks through angular momentum transport, observational evidence of magnetic fields has only been found in a small number of disks. Although dust continuum linear polarization has been detected in an increasing number of disks, its pattern is more consistent with that from dust scattering than from magnetically aligned grains in the vast majority of cases. Continuum linear polarization from dust grains aligned to a magnetic field can reveal information about the magnetic field's direction, but not its strength. On the other hand, observations of circular polarization in molecular lines produced by Zeeman splitting offer a direct measure of the line-of-sight magnetic field strength in disks. We present upper limits on the net toroidal and vertical magnetic field strengths in the protoplanetary disk AS 209 derived from Zeeman splitting observations of the CN 2–1 line. The 3σ upper limit on the net line-of-sight magnetic field strength in AS 209 is 5.0 mG on the redshifted side of the disk and 4.2 mG on the blueshifted side of the disk. Given the disk's inclination angle, we set a 3σ upper limit on the net toroidal magnetic field strength of 8.7 and 7.3 mG for the red and blue sides of the disk, respectively, and 6.2 and 5.2 mG on the net vertical magnetic field on the red and blue sides of the disk. If magnetic disk winds are a significant mechanism of angular momentum transport in the disk, magnetic fields of a strength close to the upper limits would be sufficient to drive accretion at the rate previously inferred for regions near the protostar.

Unified Astronomy Thesaurus concepts: Protoplanetary disks (1300); Magnetic fields (994); Stellar accretion disks (1579)

1. Introduction

Magnetic fields are thought to play an essential role in the evolution of protoplanetary disks by providing a means of angular momentum transport through the magnetorotational instability (MRI; Balbus & Hawley 1998) or magnetic disk winds (Blandford & Payne 1982). The MRI mechanism requires that material have a high-enough ionization fraction to be well coupled to the magnetic field. In protoplanetary disks, the ionization fraction is only expected to be high enough to produce MRI within ∼0.1 au of the central protostar, where the temperature is high enough to produce thermal ionization, and in the surface layers of the disk, where nonthermal ionization sources such as cosmic rays, X-rays (Igea & Glassgold 1999), and far-ultraviolet photons (Perez-Becker & Chiang 2011) can penetrate (Gammie 1996). The poloidal component of the disk magnetic field gives rise to the magnetic disk wind. The disk wind system modeled in Suriano et al. (2018) predicts that the disk magnetic field will have both toroidal and poloidal components, with the toroidal component being stronger than the poloidal component in regions above and below the disk midplane (see Suriano et al. 2018 Figures 4 and 5).

Observationally determining magnetic field strengths and morphologies in protoplanetary disks to constrain the various angular momentum transport mechanisms has proven difficult. The original motivation behind many millimeter and submillimeter continuum polarization observations of protoplanetary disks was to find evidence of dust grain alignment to disk magnetic fields (e.g., Rao et al. 2014; Stephens et al. 2014; Segura-Cox et al. 2015). However, the polarized emission seen in many disks at these wavelengths is better explained by dust scattering of thermal emission (e.g., Kataoka et al. 2015; Yang et al. 2016, 2017). While possible evidence of grain alignment to disk magnetic fields has been found in the circumbinary disks BHB 07–11 (Alves et al. 2018) and VLA 1623 (Harris et al. 2018; Sadavoy et al. 2018), and in the disk of HD 142527 (Ohashi et al. 2018), these observations provide information about the direction and morphology of the magnetic field lines, not the magnetic field strength.

The Zeeman effect offers a direct means of constraining the line-of-sight magnetic field strength without contamination from continuum dust scattering; however, it is possible to produce circular polarization in molecular lines through resonant scattering (Houde et al. 2013). In the presence of a magnetic field, spectral lines split apart in frequency to a degree that depends on the magnetic field strength as $\nu = \nu_0 \pm \frac{eB}{4\pi m_e c}$ (e.g., Crutcher & Kemball 2019), where ν_0 is the line frequency in the absence of a magnetic field and B is the magnetic field

strength. In astronomical sources with intrinsically weak magnetic fields compared to those in, for example, stellar photospheres, the observable for the Zeeman splitting is circular polarization of the spectral line, which measures the line-of-sight magnetic field strength. Paramagnetic species, such as the CN radical, are particularly sensitive to the Zeeman effect. CN is also one of only three species in which the Zeeman effect has been unambiguously detected in extended molecular gas in star-forming regions (Crutcher 2012). However, the Zeeman effect has yet to be detected in a protoplanetary disk, despite a recent attempt with ALMA (Vlemmings et al. 2019).

AS 209 is a protoplanetary disk located in the Ophiuchus star-forming region at a distance of 126 pc from the Sun (Gaia Collaboration et al. 2016). The protostar has a mass of 1.25 $M_\odot$ (Teague et al. 2018) and a luminosity of 1.5 $L_\odot$ (Tazzari et al. 2016). The disk is known to have two rings at $r = 75$ au and $r = 130$ au and two gaps at $r = 62$ au and $r = 103$ au (Fedele et al. 2018). This source was selected as a target source based on its inclination angle, the presence of a bright CN line (Öberg et al. 2011), and a high accretion rate of nearly $10^{-7} M_\odot$ yr^{-1} (Johns-Krull et al. 2000). The disk's inclination angle (i) of $35°.3 \pm 0°.8$ (Fedele et al. 2018), where $i = 0°$ represents a face-on disk, means that both toroidal and vertical magnetic field lines would have a component along the line of sight, with the toroidal component $B_\phi = B_{LOS} / \sin i$ along the disk's major axis and the vertical component $B_z = B_{LOS} / \cos i$. Finally, a strong magnetic field would likely be needed to drive its high accretion rate.

In this paper, we present Zeeman observations toward AS 209 using CN 2–1. In Section 2, we present the observations, including the continuum polarization. Without an obvious Zeeman detection, we then use two analysis approaches in Section 3. In Section 4, we place limits on the magnetic strength, and in Section 5, we summarize the results.

2. Observations

These observations were taken with the Atacama Large Millimeter/Submillimeter Array (ALMA). All data discussed in this paper were taken as part of ALMA project 2018.1.01030.S (PI: Rachel Harrison). The observations were taken in four execution blocs between 2019 March 6 and March 7 while the array was in configuration C43-1. The total observing time was 6.1 hr, of which 2.7 hr were spent on AS 209. The average sampling time was ∼6 s. J1733–1304 was the phase calibrator, J1751+0939 was the polarization calibrator, and J1427–4206 was the bandpass calibrator. The data set consists of two spectral line windows with a channel width of 122.070 kHz and a total bandwidth of 117.1875 MHz each, and two continuum windows with a channel width of 976.562 kHz and a total bandwidth of 937.5000 MHz each. The spectral line windows are centered on 226.64013 GHz and 226.88081 GHz. One spectral line window covered lines 1–4 listed in Table 1, and the other covered lines 5–9. The Zeeman factors for all of the lines observed are from H. Shinnaga & S. Yamamoto (2021, in preparation). Shinnaga and Yamamoto calculated the Zeeman factors under the framework of the first-order perturbation, as the interstellar magnetic field is quite weak, as weak as 100 μG or less. The authors employ the Hunds case (b) for the coupling scheme of the angular momenta for the calculation (Gordy & Cook 1970). We quote Shinnaga and Yamamoto's Zeeman factor values to the second decimal place,

Table 1
CN N $= 2 \rightarrow 1$ Hyperfine Lines

Line	$J, F \rightarrow J', F'$	ν (GHz)	Z (Hz/ μG)
1	$\frac{3}{2}, \frac{3}{2} \rightarrow \frac{1}{2}, \frac{3}{2}$	226.63217	−0.72
2	$\frac{3}{2}, \frac{5}{2} \rightarrow \frac{1}{2}, \frac{3}{2}$	226.65956	−0.71
3	$\frac{3}{2}, \frac{1}{2} \rightarrow \frac{1}{2}, \frac{1}{2}$	226.66369	−0.62
4	$\frac{3}{2}, \frac{3}{2} \rightarrow \frac{1}{2}, \frac{1}{2}$	226.67931	−1.18
5	$\frac{5}{2}, \frac{5}{2} \rightarrow \frac{3}{2}, \frac{3}{2}$	226.87419	+0.71
6	$\frac{5}{2}, \frac{7}{2} \rightarrow \frac{3}{2}, \frac{5}{2}$	226.87478	+0.40
7	$\frac{5}{2}, \frac{3}{2} \rightarrow \frac{3}{2}, \frac{1}{2}$	226.87590	+1.18
8	$\frac{5}{2}, \frac{3}{2} \rightarrow \frac{3}{2}, \frac{3}{2}$	226.88742	+1.47
9	$\frac{5}{2}, \frac{5}{2} \rightarrow \frac{3}{2}, \frac{5}{2}$	226.89213	+1.06

Note. Frequencies and Zeeman splitting factors (Z) calculated from theory for the hyperfine lines (H. Shinnaga & S. Yamamoto 2021, in preparation) covered in these observations. The Zeeman splitting factor is a measure of how much a line will be split in frequency by a given magnetic field strength. A higher absolute value of Z means that a line is more sensitive to the line-of-sight magnetic field.

and they are in agreement with those reported in Vlemmings et al. (2019).

The data were calibrated by data analysts at the NAASC using a script developed for calibrating ALMA polarization observations. All data reduction was performed using the Common Astronomy Software Applications (CASA) version 5.4.0. The data were cleaned using Briggs weighting with a robust parameter of 0.5 to create image cubes and continuum images for all four Stokes parameters. We performed one round of phase-only self-calibration on the continuum I data, with the solution interval set to the scan length. Before making the line image cubes, we subtracted the continuum emission from the spectral line windows. The image cubes were created with a spectral resolution of 0.25 km s^{-1}. The images have a beam size of $1''.40 \times 1''.27$. The linear polarized intensity map was debiased using the average noise value determined from the Q and U maps, an estimator used by, e.g., Wardle & Kronberg (1974) and Vidal et al. (2016):

$$P = \begin{cases} \sqrt{Q^2 + U^2 - \sigma^2} & \text{if } \sqrt{Q^2 + U^2} \geqslant \sigma \\ 0 & \text{otherwise.} \end{cases} \quad (1)$$

We estimate that the uncertainty on the amplitude calibration is $\pm 10\%$, and from here on, we only give statistical uncertainties. The rms values of the image cubes are $\sigma_{(I,Q,U,V)} = (0.91, 0.95, 0.96, 0.95)$ mJy beam^{-1} per 0.25 km s^{-1} channel in the spectral window containing lines 1–4 and $\sigma_{(I,Q,U,V)} = (0.95, 0.88, 0.90, 0.89)$ mJy beam^{-1} per 0.25 km s^{-1} channel in the spectral window containing lines 5–9. The continuum I rms value was 0.60 mJy beam^{-1} before self-calibration and 0.33 mJy beam^{-1} after self-calibration. The rms values for the Q, U, and V continuum images are $\sigma_{(Q,U,V)} = (0.015, 0.012, 0.013)$ mJy beam^{-1}. The higher noise value in Stokes I compared to Q, U, and V is due to dynamic range limits.

3. Results

In the dust continuum total intensity (Stokes I), the disk has a peak flux of 127.4 mJy/beam and a total intensity of 215.0 ± 1.8 mJy. All nine of the hyperfine components that
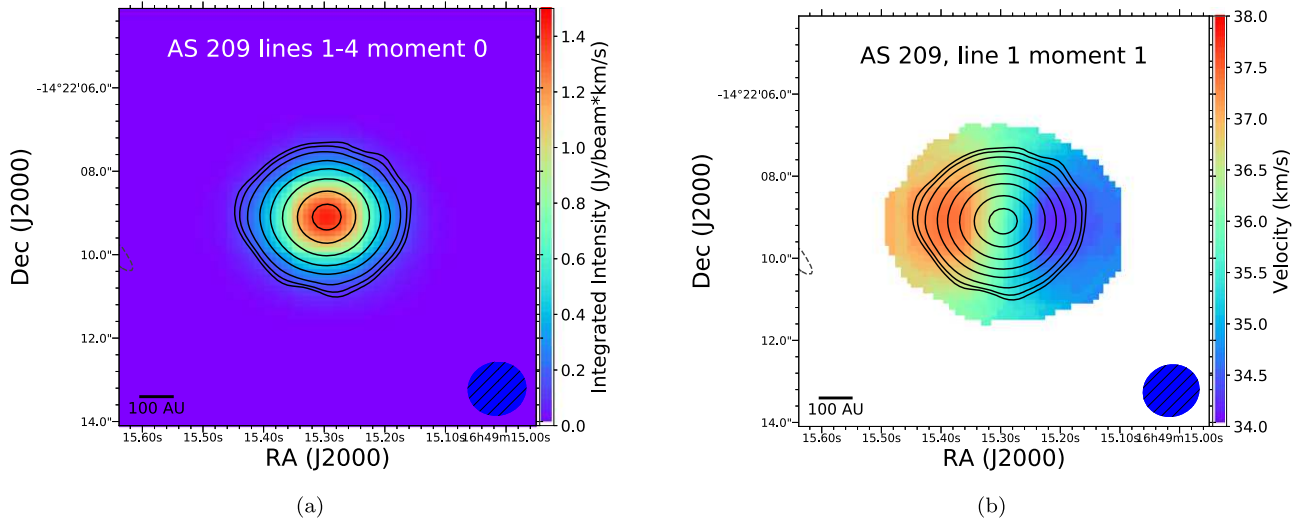
Figure 1. Integrated intensity (moment 0) map for hyperfine components 1–4 (a), and velocity (moment 1) map for hyperfine component 1 (b). The moment maps are created from line emission with intensity $\geqslant 5\sigma_{I\,\mathrm{line}}$. Contours represent total intensity (Stokes I) of 3σ, 10σ, 50σ, 100σ, 200σ, 325σ, and 500σ levels.

we targeted were detected in Stokes I. The integrated line intensity for the hyperfine components of lines 5–7 in Table 1 is 3.874 ± 0.015 Jy km s^{-1}, which is consistent with the value of 3.32 ± 0.14 Jy km s^{-1} from Öberg et al. (2011), given that the absolute flux calibration uncertainty is $\sim$10% for ALMA and $\sim$10%–15% for the SMA. The velocity map of the source shows the pattern expected from a rotating disk (see Figure 1(b)).

3.1. Line Circular Polarization

The Stokes V polarization produced by the Zeeman effect is related to the strength of the line-of-sight B field B_{LOS}, the derivative of the line Stokes I flux with respect to frequency $dI/d\nu$, and the Zeeman splitting factor Z by $V = \frac{1}{2}ZB_{\mathrm{LOS}}\frac{dI}{d\nu}$ in the case where the frequency splitting is small compared to the Stokes I line width. We made maps of all of the CN hyperfine lines in Table 1 looking for detections in Stokes V. Stokes V was not obviously detected in the channel maps, spectra, or moment 0 maps. However, the signal could be contaminated by instrumental terms. To solve for and eliminate instrumental effects that could mimic Zeeman splitting, we use the technique developed by Crutcher et al. (1996). This technique fits the observed Stokes V profile of each hyperfine component to the expression

$$V_j(\nu) = C_1 I_j(\nu) + C_2 \frac{dI_j(\nu)}{d\nu} + \frac{1}{2}BZ_j\frac{dI_j(\nu)}{d\nu}, \qquad (2)$$

where j refers to each hyperfine component. C_1 absorbs any gain difference between left and right polarization that was not calibrated out previously, as well as any linearly polarized line signal. C_2 absorbs any instrumental polarization effects such as beam squint that produce pseudo-Zeeman splitting, which shows up as the same splitting in each hyperfine line. B will be nonzero only if there is circular polarization due to the Zeeman effect. We used this method to simultaneously fit all of the unblended portions of the lines integrated over the circumstellar disk, but we were still unable to find a detection of Zeeman splitting.

However, unlike the case for the clouds studied by Crutcher et al. (1996), the disk of AS 209 is rotating, which broadens the
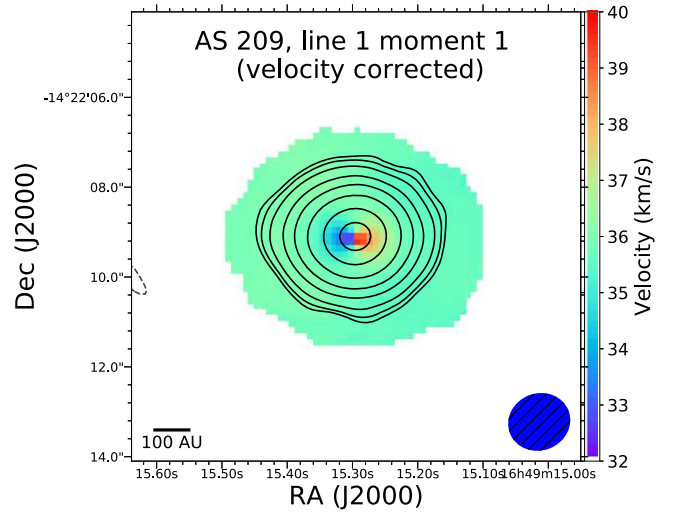

Figure 2. Velocity (moment 1) map for hyperfine 1, made using data corrected for Keplerian rotation using gofish. Contours represent total intensity (Stokes I) of 3σ, 10σ, 50σ, 100σ, 200σ, 325σ, and 500σ levels.

line emission and would impact any disk spatial averaging. To account for this, we used the package gofish (Teague 2019) to shift the velocities in the Stokes I and Stokes V cubes by the amounts appropriate to correct for Keplerian motion. Based on the disk's inclination angle, position angle, distance, and stellar mass, gofish calculates the expected Keplerian velocity for each pixel in the image cube. This allows us to shift the line emission for each Stokes parameter onto a common centroid velocity range based on the disk's deprojected Keplerian rotation profile. Teague et al. (2018) showed that AS 209's rotation profile differs from the Keplerian profile of a disk with the parameters listed in the introduction by at most $\pm$5%. For the purposes of this paper, assuming a Keplerian rotation profile is sufficient to account for the large majority of the motion within the disk. Figure 2 shows a moment 1 map created from an image cube whose pixels have been shifted along the velocity axis to correct for Keplerian motion using gofish. This velocity correction process is limited by our angular resolution. Pixels within one beam of the disk's center will contain emission from both the redshifted and blueshifted
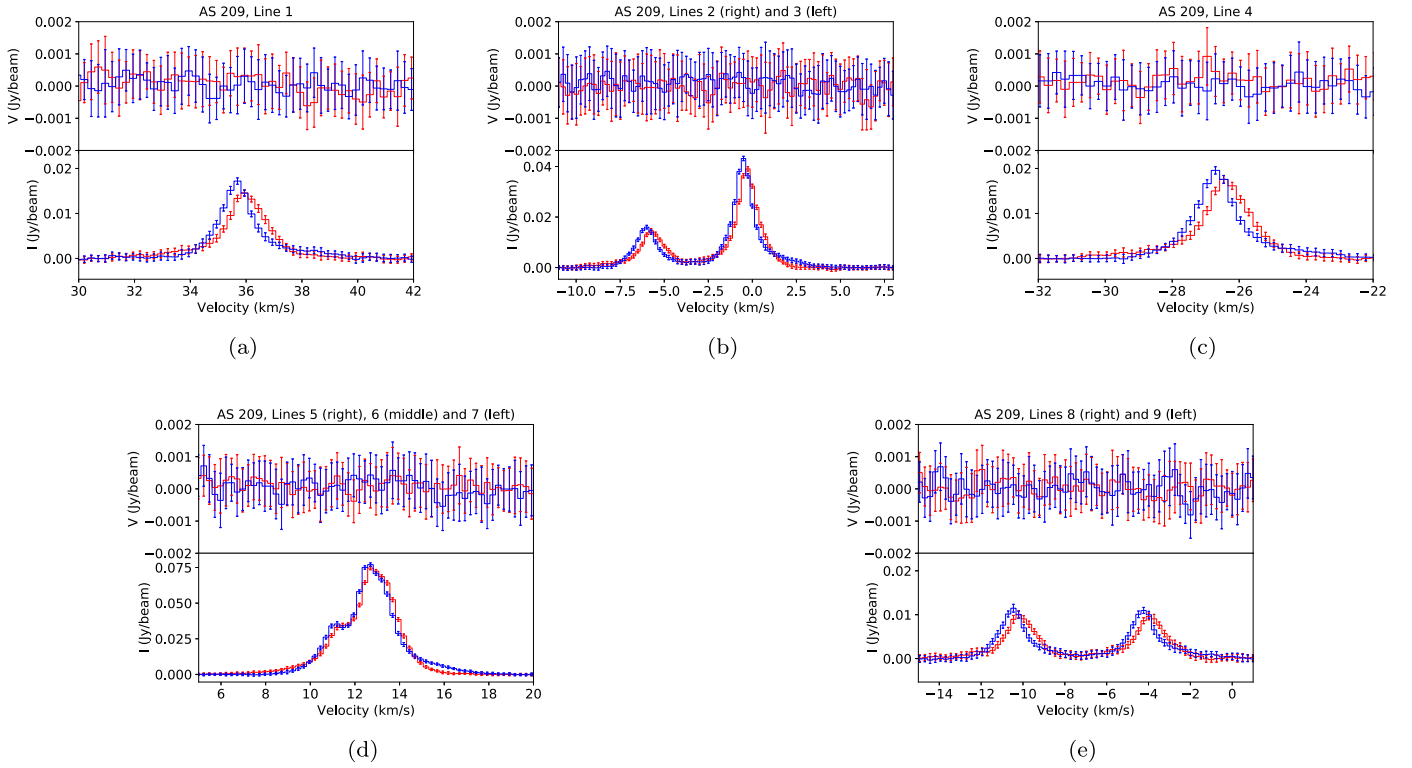
Figure 3. Stokes *V* and Stokes *I* profiles created using `gofish` for hyperfine components 1–9, averaged across the redshifted and blueshifted sides of AS 209. Velocities are LSRK velocities with respect to the velocity of hyperfine component 2. The red line represents the redshifted side of the disk, and the blue line represents the blueshifted side of the disk. The sinusoidal fluctuations in the Stokes *V* profiles are caused by the correlation of noise between velocity channels.

sides of the disk and will thus have a velocity closer to the central velocity of the line than they would in an image with infinite angular resolution. This leads to the overcorrection of the velocities near the center of the disk seen in Figure 2. We therefore exclude the region within a $0\rlap{.}''7$ radius (half of the beam major axis) of the disk's center from our fits.

Our angular resolution is sufficient to resolve the redshifted and blueshifted sides of the disk. This is advantageous for investigating any toroidal component of the magnetic field because we expect a toroidal magnetic field to have opposite signs on the red and blue sides of the disk. We used two different methods to extract information about the magnetic field in the disk. First, we created average Stokes *I* and average Stokes *V* profiles for the redshifted and blueshifted sides of the disk and fit these data using the technique described earlier in this section. The Stokes *I* and *V* spectra for all of the hyperfine components created using `gofish` are shown in Figure 3. To calculate the uncertainties in each velocity bin, we calculated the per-channel rms in a region outside the disk from spectral line cubes whose velocities had been Kepler-corrected in `gofish`.

After using `gofish` to account for line broadening due to Keplerian motion, lines 5, 6, and 7 were still blended. We therefore used only the lower-frequency portion of the Kepler-corrected line 5 data and the higher-frequency portion of the Kepler-corrected line 7 data in the Crutcher et al. (1996) fit. The magnetic field strength that produced the best fit to these data was 1.9 ± 1.7 mG on the redshifted side of the disk and 1.0 ± 1.4 mG on the blueshifted side of the disk. The value of C_1 was $-3.7 \times 10^{-3} \pm 1.1 \times 10^{-3}$ on the red side of the disk and $-4.1 \times 10^{-3} \pm 1.1 \times 10^{-3}$ on the blue side. The value of C_2 was 1.8 ± 2.3 Hz on the red side of the disk and -1.4 ± 1.9

Hz on the blue side. The Stokes *V* profiles created by Zeeman splitting are dependent on the Zeeman splitting factors, which are different for each line, making it unlikely that an instrumental effect like beam squint (which would affect all lines in the same way) could destroy a real Zeeman signal. The uncertainty of $0\rlap{.}°8$ on the disk's inclination angle adds an additional 0.07 mG to the 1σ error bar on the net line-of-sight magnetic field strength on the redshifted side of the disk, and 0.03 mG on the blueshifted side of the disk. For the remainder of this paper, we will deal with the upper limits derived using an assumed inclination angle of $35\rlap{.}°3$. Using the uncertainties on the magnetic field strengths as the 1σ value, the limit on the net line-of-sight magnetic field strength is 5.0 mG on the redshifted side of the disk and 4.2 mG on the blueshifted side of the disk. Given the disk's inclination angle of $35\rlap{.}°3$, this places 3σ upper limits of 8.7 mG (red) and 7.3 mG (blue) on the net toroidal magnetic field and 6.3 mG (red) and 5.1 mG (blue) on the net vertical magnetic field. The Stokes *I* and *V* averaged spectra from the red and blue sides of each line are shown in Figure 3.

Second, we stacked (i.e., summed) the Stokes *I* and Stokes *V* spectra from both the red and blue sides of the disk for only the unblended lines. The Stokes *I* spectra were scaled by their relative intensities, and the Stokes *V* spectra were scaled by the relative Stokes *I* intensities and the Zeeman splitting factors. If the disk field is toroidal, we would expect the Stokes *V* spectrum from one side of the disk to be the same shape as the spectrum from the other side of the disk, but mirrored across the velocity axis. This is because the line-of-sight component of a toroidal field would have opposite signs on the redshifted and blueshifted sides of the disk, and $V(v)$ is proportional to the line-of-sight component of B_z, including the sign. Therefore,
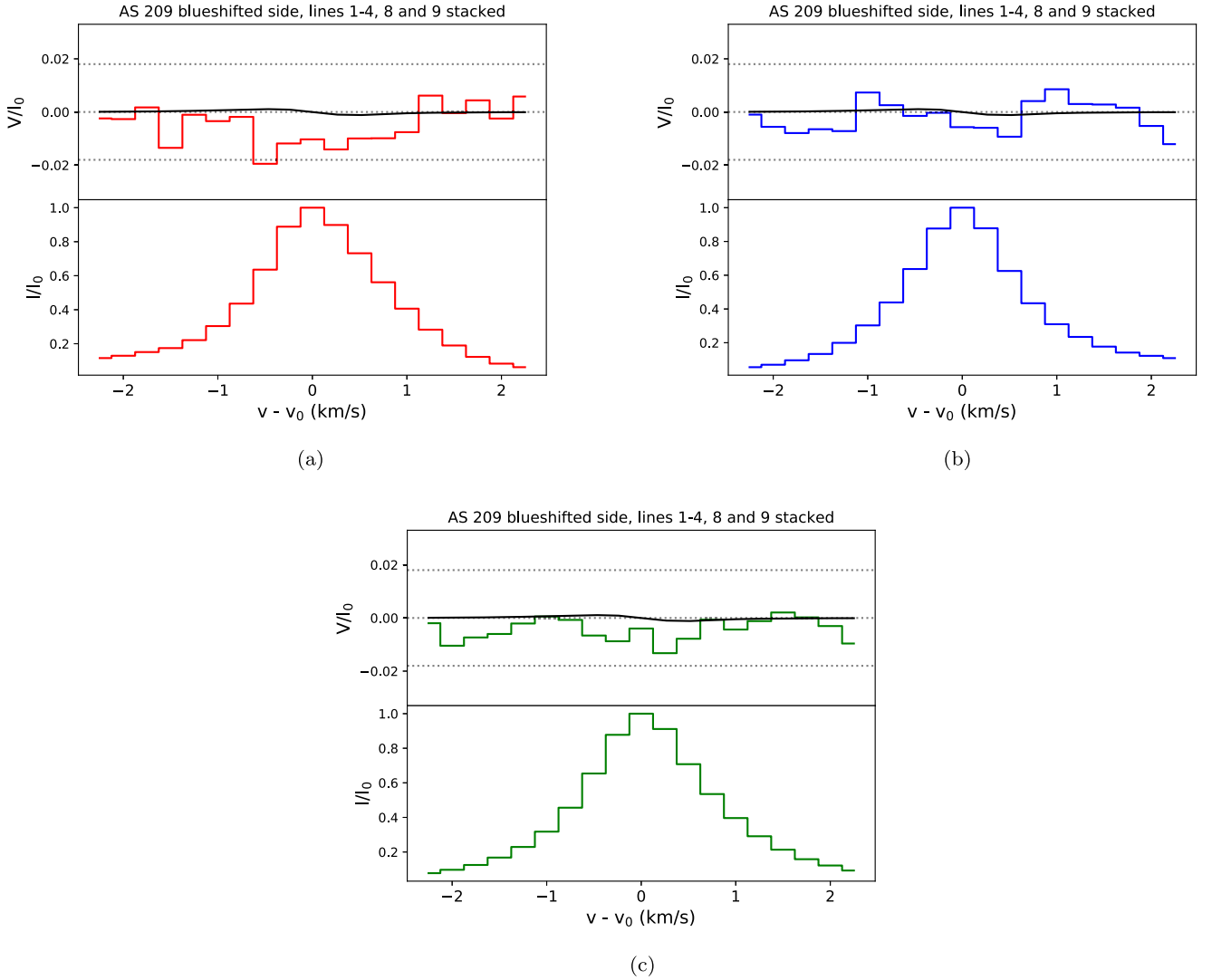
(a)

(b)

(c)

Figure 4. Stacked Stokes I and V spectra using `gofish` for the redshifted (a) and blueshifted (b) sides of the disk, and for the full disk (c). The black lines represent the best fit of the equation $V = \frac{1}{2} Z B_{\mathrm{LOS}} \frac{dI}{d\nu}$ to the data. The dashed horizontal lines in the plots of V/I_0 represent $\pm 1.8\%$ of the I/I_0 peak.

stacking $V(v)$ from the red side of the disk with $-V(v)$ from the blue side of the disk should increase the signal-to-noise ratio of any Stokes V emission that comes from a toroidal field. However, this method of stacking would destroy any Stokes V signal from a vertical magnetic field, as we expect the direction of the vertical component of the field to remain the same across the disk. Nonetheless, stacking the lines in this way did not lead to a detection of circularly polarized emission. We fit the weighted sum of the line profiles $V_{\mathrm{tot}} = \frac{1}{2I_0} B_{\mathrm{los}} \sum_i Z_i \frac{dI_i}{d\nu_i} w_I w_Z$ to the stacked line data, where the i's are lines 1, 2, 3, 4, 8, and 9; I_0 is the maximum Stokes I intensity, and w_I and w_Z are weighting factors that account for the relative intensities of the lines and the relative strengths of their Zeeman splitting factors, respectively. The stacked spectra are shown in Figure 4. The best-fit values for B_{los} from this stacking technique were -4.2 ± 6.9 mG for the redshifted side of the disk, 2.0 ± 4.6 mG for the blueshifted side of the disk, and 0.4 ± 4.9 mG for the full disk. Because this method does not account for circular polarization from instrumental effects, we report the results of using the first fitting technique described above as our final upper limits on the magnetic field strength.

3.2. Continuum Linear Polarization

The continuum polarization pattern in AS 209 at 1.3 mm is shown in Figure 5. Our observations are similar to those observed at 870 μm by Mori et al. (2019), with the direction of polarization oriented parallel to the disk's minor axis in the inner part of the disk and oriented azimuthally in the outer part of the disk. This pattern closely matches the polarization from scattering in a disk with a similar inclination to AS 209's predicted by the model in Yang et al. (2016). We plan to explore the possible mechanisms behind this polarization pattern in a future paper.

4. Discussion

We did not detect circular polarization in any of the individual CN 2–1 lines or in the stacked lines, so we have calculated 3σ upper limits on the net toroidal and vertical magnetic field strengths. The minimum detectable degree of circular polarization with ALMA is 1.8% of the peak Stokes I flux according to the ALMA Cycle 7 Technical Handbook. The Stokes V flux does not reach this 1.8% threshold in any channel of any individual hyperfine line or the stacked lines in our
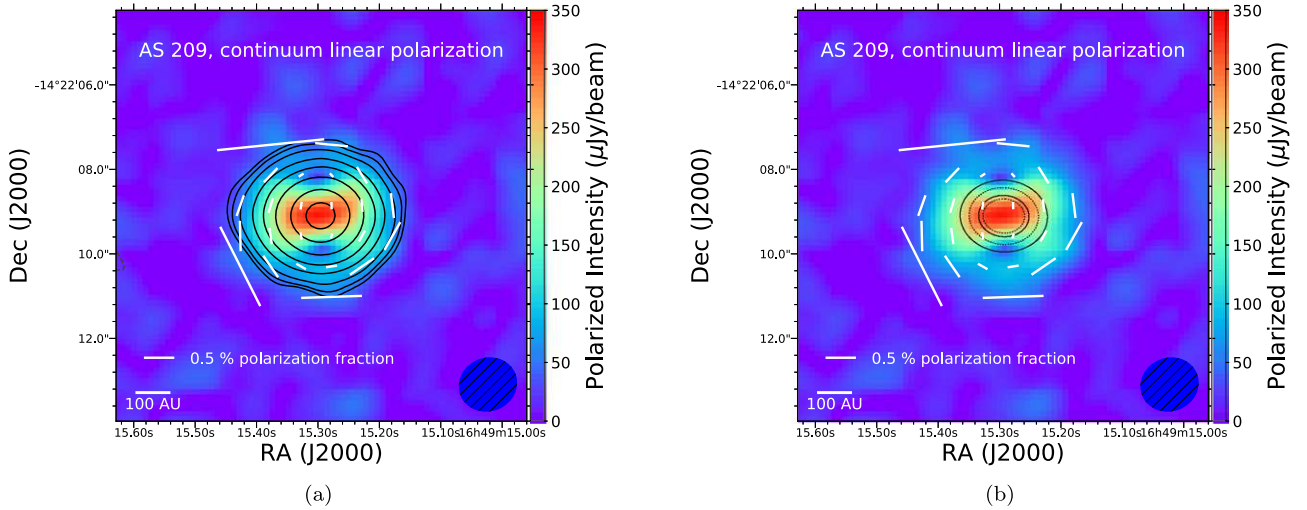
Figure 5. 1.3 mm continuum linear polarization in AS 209. The black contours in (a) represent total intensity (Stokes I) of 3σ, 10σ, 50σ, 100σ, 200σ, 325σ, and 500σ levels. The solid contours in (b) represent the locations of rings, and the dashed contours represent the locations of gaps from Fedele et al. (2018). The color map represents debiased polarized intensity with the scale on the right of each source. The length of the polarization vectors corresponds to the polarization fraction. The vectors are plotted with ∼5 segments per beam. Vectors are only plotted where the polarized intensity $P \geqslant 3\sigma_P$ and $P/I \geqslant 0.1$.

observations. Because the fitting technique described in Section 3.1 removes instrumental effects that could produce spurious Stokes V signal, and because the Stokes V spectrum is noise-like, the uncertainties on the magnetic field strengths calculated using the fitting technique can be used to calculate upper limits on the disk's magnetic field strength. The average rms values on the Stokes V spectra shown in Figure 3 were ∼0.9% of the Stokes I peak of the brightest line, which means that a Stokes V signal $\geqslant$0.02 Jy beam^{-1} would be detectable in the brightest line. Here, we discuss the implications of our field strength upper limits for the disk's mass accretion rate, as well as possible reasons for the non-detection.

Our no-detection of Zeeman splitting in the CN 2–1 line allows us to put constraints on the mass accretion rate that the magnetic field can drive in the disk on the tens of au scale. The magnetically driven accretion rate $\dot{M}_{\mathrm{mag}}$ is related to the magnetic stresses through, e.g., Equation (18) of Wang et al. (2019). Making the simplifying assumptions that $|B_R|$, $|B_z|$, and $|B_\phi|$ are constant, and that B_ϕ has opposite signs above and below the midplane, this equation can be recast into a rough order-of-magnitude estimate of the magnetically driven accretion rate:

$$\dot{M}_{\mathrm{mag}} \approx \frac{2R}{\Omega}|B_z B_\phi| + \frac{2h}{\Omega}|B_R B_\phi|$$
$$= \frac{2R|B_z B_\phi|}{\Omega}\left(1 + \frac{h}{R}\frac{|B_R|}{|B_z|}\right), \qquad (3)$$

where B_R, B_z, and B_ϕ are, respectively, the (cylindrically) radial, vertical and azimuthal components of the magnetic field, h the disk scale height, and $\Omega = (GM_*/R^3)^{1/2}$ is the angular Keplerian speed at radius R. The first term on the right-hand side of the equation is mass accretion driven by a magnetized disk wind and the second term is that from magnetic stresses internal to the disk. They are consistent with the estimates from Bai & Goodman (2009; see their Equations (6) and (15), respectively). Because the disk is geometrically thin, with $h/R \ll 1$, the magnetic disk wind tends to remove angular momentum more efficiently than the internal magnetic stresses

for comparable B_z and B_R. In this case, we have

$$\dot{M}_{\mathrm{mag}} \approx \frac{2R|B_z B_\phi|}{\Omega} = 2.1 \times 10^{-6}\left(\frac{|B_z|}{6.2\ \mathrm{mG}}\right)\left(\frac{|B_\phi|}{8.7\ \mathrm{mG}}\right)$$
$$\times \left(\frac{M_*}{1.25\ M_\odot}\right)^{-1/2}\left(\frac{R}{50\ \mathrm{au}}\right)^{5/2}\frac{M_\odot}{\mathrm{yr}}, \qquad (4)$$

where we have normalized the vertical and toroidal components of the magnetic field by their respective 3σ upper limits and the stellar mass M_* by the value inferred in Teague et al. (2018). The ∼$10^{-6}\,M_\odot$ yr^{-1} value we estimate from our magnetic field strength upper limits is to be compared with the mass accretion rate from the disk onto the central star of 10^{-7} $M_\odot$/yr estimated by Johns-Krull et al. (2000) based on the luminosity of ultraviolet lines (especially CIV). This accretion rate is on the high side for classical T Tauri stars and needs to be checked through independent methods.

It is possible that the absolute value of the disk magnetic field strength $|B|$ is substantially higher than our upper limits on the net line-of-sight magnetic field strength. This is particularly true in the case where the magnetic field in the disk is dominated by the toroidal component B_ϕ, and B_ϕ reverses polarity across the disk midplane. Such a field reversal would be naturally produced if there is a net magnetic flux threading the disk (as is likely given that the disk forms out of magnetized dense cores that appear to have fairly regular magnetic fields as traced by dust polarization; for a recent review, see Hull & Zhang 2019). The differential rotation between the disk midplane and the atmosphere and/or disk wind naturally twists the poloidal field into a toroidal field that reverses direction around the midplane (for an illustration, see Suriano et al. 2018). In this case, if the disk is not too optically thick, an individual line of sight will contain CN emission from above and below the disk midplane and thus sample gas with reversed toroidal magnetic fields and thus Zeeman signals of opposite sign. The optical depths of the bright rings of AS 209 are estimated to be 0.46 and 0.52 at ALMA Band 6 (Dullemond et al. 2018) and should be much lower in the gaps. It is likely that the bulk of the CN-emitting materials both

above and below the disk midplane contribute to the observed signals, which leads to a cancellation of the Zeeman signal. In this case, the Zeeman measurement can significantly underestimate the absolute strength of the magnetic field, as illustrated quantitatively by Mazzei et al. (2020).

5. Conclusions

We present the first Zeeman observations toward the circumstellar disk of AS 209, using nine hyperfine components of CN 2–1 in ALMA Band 6. Although we easily detect the dust polarization of the disk, which is consistent with previous Band 7 observations, we do not detect any polarized emission in the CN lines. After correcting for the Keplerian rotation of the disk using gofish, we used two approaches to derive upper limits on the magnetic field strengths: fitting the equation described in Equation (2) to each hyperfine component as described in Crutcher et al. (1996) and fitting an equation with the form of the Zeeman splitting profile to the scaled sum of all of the unblended components. We derived these limits for the redshifted and blueshifted sides of the disk, as well as the entire disk. We present 3σ upper limits based on the stacking technique described in Crutcher et al. (1996) because this technique allows us to remove circular polarization from instrumental effects from the Stokes V spectra. In that case, we have calculated 3σ upper limits on the net toroidal and vertical magnetic field strengths of $B_\phi < 8.7$ mG and $B_z < 6.1$ mG. A change in polarity of the toroidal magnetic field across the disk midplane may cause us to underestimate the absolute strength of the toroidal component of the magnetic field, and therefore, the true toroidal magnetic field strength could be >8.7 mG. Our constraints on the magnetic field strength provide an upper limit on the magnetically driven mass accretion rate on the 50 au scale of order 10^{-6} $M_\odot$ yr^{-1} or smaller, which is consistent with the mass accretion rate onto the star previously inferred for this object.

ORCID iDs

Rachel E. Harrison ⬥ https://orcid.org/0000-0003-2118-4999
Leslie W. Looney ⬥ https://orcid.org/0000-0002-4540-6587
Ian W. Stephens ⬥ https://orcid.org/0000-0003-3017-4418
Richard Teague ⬥ https://orcid.org/0000-0003-1534-5186
Haifeng Yang ⬥ https://orcid.org/0000-0002-8537-6669
Erin G. Cox ⬥ https://orcid.org/0000-0002-5216-8062
Manuel Fernández-López ⬥ https://orcid.org/0000-0001-5811-0454
Hiroko Shinnaga ⬥ https://orcid.org/0000-0001-9407-6775

References

Alves, F. O., Girart, J. M., Padovani, M., et al. 2018, A&A, 616, A56
Bai, X.-N., & Goodman, J. 2009, ApJ, 701, 737
Balbus, S. A., & Hawley, J. F. 1998, RvMP, 70, 1
Blandford, R. D., & Payne, D. G. 1982, MNRAS, 199, 883
Crutcher, R. M. 2012, ARA&A, 50, 29
Crutcher, R. M., & Kemball, A. J. 2019, FrASS, 6, 66
Crutcher, R. M., Troland, T. H., Lazareff, B., & Kazes, I. 1996, ApJ, 456, 217
Dullemond, C. P., Birnstiel, T., Huang, J., et al. 2018, ApJL, 869, L46
Fedele, D., Tazzari, M., Booth, R., et al. 2018, A&A, 610, A24
Gaia Collaboration, Brown, A. G. A., Vallenari, A., et al. 2016, A&A, 595, A2
Gammie, C. F. 1996, ApJ, 457, 355
Gordy, W., & Cook, R. L. 1970, Microwave Molecular Spectra, Chemical Applications of Spectroscopy (New York: Wiley)
Harris, R. J., Cox, E. G., Looney, L. W., et al. 2018, ApJ, 861, 91
Houde, M., Hezareh, T., Jones, S., & Rajabi, F. 2013, ApJ, 764, 24
Hull, C. L. H., & Zhang, Q. 2019, FrASS, 6, 3
Igea, J., & Glassgold, A. E. 1999, ApJ, 518, 848
Johns-Krull, C. M., Valenti, J. A., & Linsky, J. L. 2000, ApJ, 539, 815
Kataoka, A., Muto, T., Momose, M., et al. 2015, ApJ, 809, 78
Mazzei, R., Cleeves, L. I., & Li, Z.-Y. 2020, ApJ, 903, 20
Mori, T., Kataoka, A., Ohashi, S., et al. 2019, ApJ, 883, 16
Öberg, K. I., Qi, C., Fogel, J. K. J., et al. 2011, ApJ, 734, 98
Ohashi, S., Kataoka, A., Nagai, H., et al. 2018, ApJ, 864, 81
Perez-Becker, D., & Chiang, E. 2011, ApJ, 735, 8
Rao, R., Girart, J. M., Lai, S.-P., & Marrone, D. P. 2014, ApJL, 780, L6
Sadavoy, S. I., Myers, P. C., Stephens, I. W., et al. 2018, ApJ, 859, 165
Segura-Cox, D. M., Looney, L. W., Stephens, I. W., et al. 2015, ApJL, 798, L2
Stephens, I. W., Looney, L. W., Kwon, W., et al. 2014, Natur, 514, 597
Suriano, S. S., Li, Z.-Y., Krasnopolsky, R., & Shang, H. 2018, MNRAS, 477, 1239
Tazzari, M., Testi, L., Ercolano, B., et al. 2016, A&A, 588, A53
Teague, R. 2019, JOSS, 4, 1632
Teague, R., Bae, J., Birnstiel, T., & Bergin, E. A. 2018, ApJ, 868, 113
Vidal, M., Leahy, J. P., & Dickinson, C. 2016, MNRAS, 461, 698
Vlemmings, W. H. T., Lankhaar, B., Cazzoletti, P., et al. 2019, A&A, 624, L7
Wang, L., Bai, X.-N., & Goodman, J. 2019, ApJ, 874, 90
Wardle, J. F. C., & Kronberg, P. P. 1974, ApJ, 194, 249
Yang, H., Li, Z.-Y., Looney, L., & Stephens, I. 2016, MNRAS, 456, 2794
Yang, H., Li, Z.-Y., Looney, L. W., Girart, J. M., & Stephens, I. W. 2017, MNRAS, 472, 373